# Non-isothermal initial stage sintering strain model with application to 316L stainless steel

S. Johnston[†], R. Anderson[†,‡], and D. Storti[†]

[†]Dept. of Mechanical Engineering, University of Washington-Seattle, 98195-2600
[‡]Concurrent Technologies Corporation, Bremerton, WA 98312

Reviewed, accepted August 3, 2005

Abstract

This research presents a study of initial stage sintering of 316L stainless steel components produced by Three-Dimensional Printing (3DP™). Current practice for the 3DP™ sintering process involves only initial stage sintering during which necks grow between the powder particles. We present a non-isothermal sintering model of neck growth that is capable of quantitative predictions within 20% of final sintering strain for 3DP™ components. The sintering model is based on the two-particle geometry where the neck geometry evolves by material transport mechanisms. Dilatometry experimentation using varied heating rates to elevated temperatures were used to determine model parameterization and fitting. The model is not entirely specific to 3DP™ components and the approach is extendable to general initial stage sintering of powder metal components.

## 1 Introduction

The ability to manufacture components from powder materials (P/M) with precise dimensional control is desirable in industry. Production of P/M components usually requires the additional process of sintering (initial or final stage) to create and increase green component strength which also produces dimensional change (sintering strain). A quantitative predictive tool that describes the dimensional change during sintering is desired; but current theoretical models are only able to predict dimensional change to within 200% of measured strain [1] and initial stage sintering is most fundamentally understood only under isothermal sintering conditions [2]. There is a need for a more accurate model of initial stage sintering that can be used for non-isothermal sintering conditions and is more accurate than current models.

The development of a non-isothermal sintering strain model that simulates the initial stage sintering of a row of spherical powder particles is presented herein. The sintering strain model is based on the two particle geometry, uses fewer geometric assumptions than previous researchers, and allows for interaction between the surface and bulk sintering mechanisms. A parametric calibration and testing of the developed sintering model has been performed by dilatometer experimentation using 316L stainless steel samples manufactured by a three dimensional printing (3DP™) process (ProMetal).

Model development began with rigourously defining the two particle geometry and volume of the neck region using basic geometric assumptions. Material transport from the individual powder particles to the neck region have been defined kinetically in terms of mechanistic

sintering fluxes. Therefore the sintering model is based on thermally activated transport mechanisms that instigate material movement to the neck volume between adjacent powder particles.

## 2 Two Particle Geometric Formulation

The first step in development of the geometric sintering model involved defining the physical geometric system. The ideal two particle model (Figure 1a) is typically used as the geometric configuration for initial stage sinter modeling. The geometric assumptions used in this analysis for the ideal two particle configuration shown in Figure 1a have been used by past researchers [1, 3, 4, 5, 6, 7]: (1) the powder particles are perfectly spherical and remain perfectly spherical during sintering, (2) adjacent particles possess the same diameter, (3) the initial contact between the particles is produced from metallic bonding forces and forms an initial neck radius, $\rho_o$ (defined as a Hertzian contact [8, 9]), (4) the neck surface remains toroidal and tangent to both powder particles, and (5) the total volume of the two particle system remains constant. The reasonableness of these geometric assumptions during initial stage sintering have been established by Exner [3].

Table 1: Parameter definitions for two particle geometry shown in Figure 1.

| Parameter | Definition | Parameter | Definition |
|---|---|---|---|
| $a$ | powder particle radius | $X$ | neck size |
| $h$ | inter particle penetration | $\rho$ | neck radius |
| $l$ | particle separation distance | $\frac{X}{a}$ | neck size ratio |

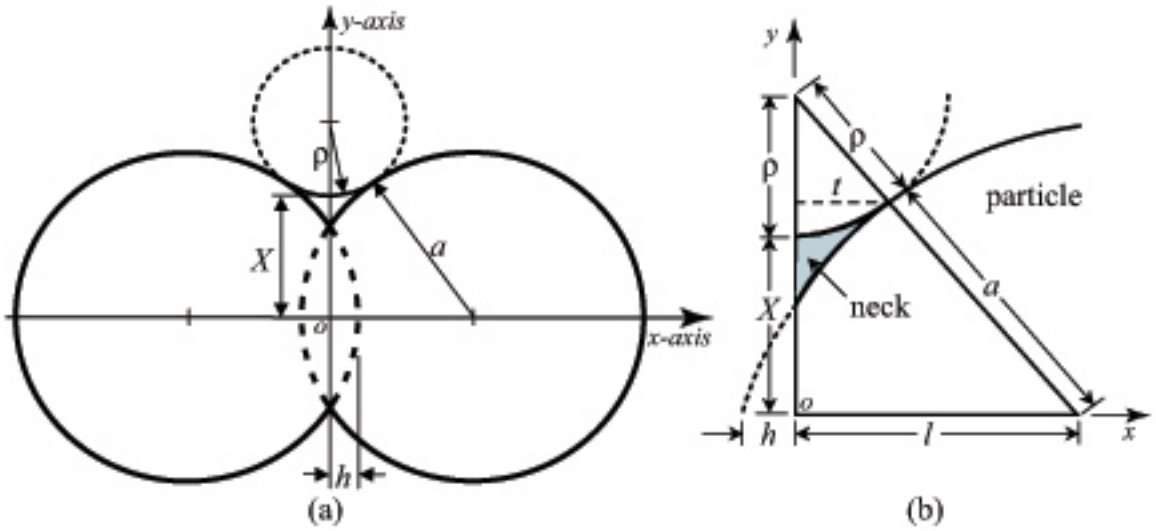


Figure 1: (a) Cross section of ideal two particle model geometry with circular neck cross section, (b) enlarged view of the neck region for the defined geometry. Geometric parameters are defined in Table 1.

The volume of the neck region can be exactly computed by using the above geometric assumptions. Figure 1b shows a 2-dimensional cross section of half the neck region, where the volume of the neck is determined by computing twice the shaded area revolved about the $x$-axis. The entire volume of the neck ($V \equiv V_{neck}$) has been defined in terms of the geometric parameters: particle radius ($a$), neck radius ($\rho$), and particle separation distance ($l$). The exact expression for the neck volume is

$$\begin{aligned} V(a,\rho,l) = &-2\pi a^2 l + \frac{2}{3}\pi l^3 + \frac{2\pi}{(a+\rho)^3}\left[la^5 - \frac{2}{3}a^3l^3 + 2a^4l\rho + 2a^3l\rho^2 - \frac{2}{3}l^3\rho^3\right] \\ &+ \frac{2\pi}{a+\rho}\left[a^2l\rho - l^3\rho + 2al\rho^2 + 2l\rho^3 - l\rho\sqrt{(a+\rho)^2 - l^2}\,\sqrt{\rho^2 - \frac{l^2\rho^2}{(a+\rho)^2}}\,\right] \\ &- 2\pi\rho^2\sqrt{(a+\rho)^2 - l^2}\,\tan^{-1}\left[\frac{l\rho}{a+\rho}\cdot\left(\sqrt{\rho^2 - \frac{l^2\rho^2}{(a+\rho)^2}}\right)^{-1}\right] \end{aligned} \tag{1}$$

The two particle neck geometry is dynamic (i.e., continuously changing with respect to time) as the sinter bond evolves, so the geometry shown in Figure 1b represents an instantaneous image of the neck geometry. The three geometric parameters ($a$, $\rho$, and $l$) evolve over time subject to a relationship corresponding to a constant volume constraint.

# 3 Sintering Mechanistic Flux Formulation

Sintering activity is characterized by atomistic movement producing a reduction of free surface energy [2, 1, 3, 5]. Atoms on the surface are not completely surrounded by neighboring atoms leaving free bond areas. These atoms with free bonds possess a higher energy state than interior atoms which gives rise to a surface energy, $\gamma$ (J/m$^2$) [2]. The free surface energy is thermally activated and then converted to material transport on and within the powder particle to areas with high curvature gradients, i.e., contacting surfaces between powder particles. The material (atoms) deposit in new locations by different sintering mechanisms forming a neck between the two particles. For spherical particles the minimized free surface forms a neck contour with a circular cross section. The atomistic material movement process can be mathematically formalized by reviewing the work of Exner [3], Johnson [5], Ashby [1], and German [2, 10], but for a complete derivation of the sintering equations, please refer to Kuczynski [11] and Kingery [12].

The current understanding of initial stage sintering involves neck growth between powder particles and is separated into two different classes of sintering mechanisms: surface transport and bulk transport. Material transport paths are shown by the dotted lines in Figure 2 for the dominating transport mechanisms. Surface transport mechanisms involve atomistic movement along the surface or near the surface of the particle, but these mechanisms do not create any dimensional change in the physical relationship of the particles (i.e., surface mechanisms do not cause shrinkage) [2, 3]. Surface transport mechanisms are also the dominating mechanisms for inter particle adhesion (neck growth) because atomistic movement starts and ends on the surface [2]. Bulk transport mechanisms influence neck growth by atomistic movement inside the particle, which produces interparticle penetration and particle approach, i.e.,

strain. Surface diffusion has been shown to be the dominating surface mechanism for neck growth [2, 13]; additionally, volume diffusion and grain boundary diffusion have been identified as the dominating bulk mechanisms producing strain [5, 14]. Ashby [1] has stated that in order to preserve the curvature driving force, material on the surface of the neck must be redistributed; thus the surface mechanism of volume diffusion on the surface (VDS) is required.

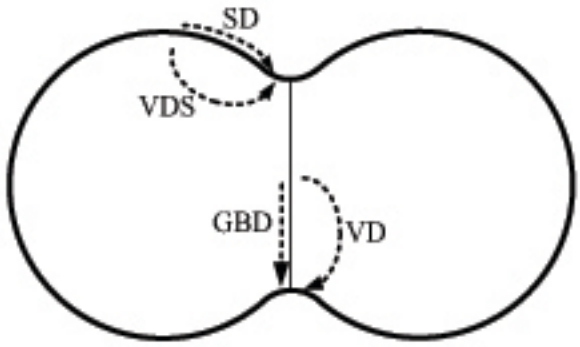


Figure 2: Atomistic material transport paths to the neck for the ideal spherical two-particle model of initial stage sintering. Surface Mechanisms: surface diffusion (SD) and volume diffusion on the surface (VDS). Bulk Mechanisms: volume diffusion (VD) and grain-boundary diffusion (GBD).

The volumetric rate of material movement for each sintering mechanism to the neck volume is defined as the product of the flux and the area over which the flux is applied

$$\dot{V}_i = J_i \cdot A_i \tag{2}$$

where the subscript $i$ indicates the sintering mechanism, $V$ is the neck volume, $J_i$ is the sintering mechanism flux, and $A_i$ is the total area to related to the flux (as formulated by Ashby [4] and Hwang [6]). The value of the surface area $A_i$ is defined to either be $A_r$ or $A_{neck}$, where $A_r$ is the area of the annulus with outer radius $X$ (shown in Figure 1) and thickness $\delta_s$ (the effective surface thickness) where the particle surface meets the neck surface

$$A_r = 2\pi X \delta_s \tag{3}$$

and $A_{neck}$ is defined as the surface area of the toroidal neck

$$A_{neck} = 2\pi\rho \left[ (X+\rho) \arcsin\left(\frac{l}{a+\rho}\right) - \frac{\rho\, l}{a+\rho} \right] \tag{4}$$

The volumetric neck growth rates for surface diffusion, volume diffusion on the surface, volume diffusion, and grain boundary diffusion are defined in Equations 5-8.

1. Surface diffusion:

$$\dot{V}_{sd} = J_{sd} \cdot A_r = \frac{B_{sd}\, D_s \gamma \Omega}{kT} \cdot \frac{1}{\rho}\left(\frac{1}{\rho} - \frac{1}{X} + \frac{2}{a}\right) \cdot A_r \tag{5}$$

2. Volume diffusion along the surface:

$$\dot{V}_{vds} = J_{vds} \cdot A_{neck} = \frac{B_{vds}\ D_v \gamma \Omega}{kT} \cdot \frac{1}{\rho}\left(\frac{1}{\rho} - \frac{1}{X} + \frac{2}{a}\right) \cdot A_{neck} \tag{6}$$

3. Volume diffusion:

$$\dot{V}_{vd} = J_{vd} \cdot A_{neck} = \frac{4B_{vd}\ D_v \gamma \Omega}{kT} \cdot \left(\frac{X+\rho}{\rho\ X^2}\right) \cdot A_{neck} \tag{7}$$

4. Grain boundary diffusion:

$$\dot{V}_{gbd} = J_{gbd} \cdot A_r = \frac{4B_{gbd}\ D_g \gamma \Omega}{kT} \cdot \left(\frac{X+\rho}{\rho\ X^2}\right) \cdot A_r^* \tag{8}$$

where $A_r^* = 2\pi r \delta_b$ ($\delta_b$ is the effective grain boundary thickness).

The neck size ($X$) can be explicitly defined in terms of $a$, $\rho$, and $l$ by using the Pythagorean Theorem (see Figure 1b).

$$X = -\rho + \sqrt{(a+\rho)^2 - l^2} \tag{9}$$

Note that the material flow rates are stated in their most concise form (depending on $a, \rho$, and $X$), and using Eq. 9, the material flow rate can be expressed in terms of $a, \rho$, and $l$ (along with the temperature and material constant parameters). The numeric factor $B_i$ for each sintering mechanism ($B_{sd}$ for surface diffusion, $B_{vd}$ for volume diffusion, etc., where $\vec{B}_i = (B_{vd}, B_{gbd}, B_{sd}, B_{vds})$ ) in Equations 5-8 have been determined by previous researchers using isothermal dilatometry results.

Table 2: Material property symbols and values for 316L stainless steel [2, 1].

| | | | | | |
|---|---|---|---|---|---|
| $D_v$ | Volume diffusivity | $4 \times 10^{-4}$ [$m^2/s$] | $Q_v$ | VD Act. energy | 280 [kJ/mol] |
| $D_s$ | Surface diffusivity | 0.4 [$m^2/s$] | $Q_s$ | SD Act. energy | 250 [kJ/mol] |
| $D_b$ | Grain bound. diff. | $4 \times 10^{-13}$ [$m^2/s$] | $Q_b$ | GBD Act. energy | 167 [kJ/mol] |
| $\delta_s$ | Surface thickness | $2.75 \times 10^{-10}$ [m] | $\delta_b$ | Grain bound. width | 10-47.5 [m] |
| $\Omega$ | Atomic volume | $1.155 \times 10^{-29}$ $\left[\frac{m^3}{atom}\right]$ | $\gamma$ | Surface energy | 2 [$J/m^2$] |

Neck growth occurs from material transported to the neck region by all of the sintering mechanisms. The total volumetric neck growth rate ($\dot{V}_{total}$) is the sum of all of the mechanistic fluxes

$$\dot{V}_{total} = \sum J_i \cdot A_i \tag{10a}$$

$$= \dot{V}_{surf} + \dot{V}_{bulk} \tag{10b}$$

where $\dot{V}_{surf}$ and $\dot{V}_{bulk}$ represent the volumetric rate for surface and bulk mechanisms, respectively.

# 4 Sintering Model

The general form of the sintering model is based on the volumetric neck growth rate of the geometric configuration defined in Section 2 and the thermally driven mechanistic fluxes defined in Section 3. The mechanistic fluxes are driven by the applied temperature profile which alters the geometry of the two particle system by changing the neck volume. The general sintering model uses two sintering foundations: (1) conservation of mass and (2) surface sintering mechanisms preserve interparticle spacing.

## 4.1 Sintering Model Formulation

The first foundation, conservation of mass, does not allow any material to be added to the two particle system. A solid state sintering process using an inert atmosphere does not produce any chemical reactions between the gas and powder particles, therefore sintering is basically a rearrangement (movement) of material (atoms) within the powder particles to the neck region. There is no gain in mass which implies that the total volume of the system $V_{sys}$) remains constant. Therefore, the volume at any instant during sintering must be equal to the initial volume of the system ($V_o$)

$$V_{sys}(a,\ \rho,\ l) = V_{sys}(a_o,\ \rho_o,\ l_o) = V_o \tag{11}$$

with initial conditions ($a_o,\ \rho_o,\ l_o$). Eq. 11 represents the first equation in the general sintering model.

The volume conservation constraint allows elimination of a variable ($\rho$) so that the expression for the neck volume (Eq. 1) can be expressed in terms of the particle radius $a$ and particle separation $l$. Therefore, the volume of the neck (Eq. 1) is now expressed as

$$V(a,\rho,l)|_{V_o} \equiv V(a,\ l) \tag{12}$$

To relate the volume of the neck under a constant volume constraint to the mechanistic volumetric rates (Equations 5-8), the total time derivative of the neck volume (Eq. 12) is computed.

$$\frac{d}{dt}V(a,l) = \frac{\partial V}{\partial a}\cdot\dot{a} + \frac{\partial V}{\partial l}\cdot\dot{l} \tag{13}$$

The total rate of change in the volume of the neck is equal to the sum of all of the volumetric mechanistic fluxes, (Section 3), thus setting Equations 10b and 13 equal to each other provides the relationship between the neck geometry and the driving mechanistic fluxes

$$\frac{\partial V}{\partial a}\cdot\dot{a} + \frac{\partial V}{\partial l}\cdot\dot{l} = \dot{V}_{surf} + \dot{V}_{bulk} \tag{14}$$

Equation 14 represents the second equation in the general sintering model.

The second foundation states that surface mechanisms preserve interparticle spacing. It is well documented in literature that the surface mechanisms do not produce sintering strain or alter the interparticle distance [1, 2, 4, 10, 13]. Restating this in terms of the geometric

parameters implies that the surface mechanisms do not change the value of $l$ during sintering, or $\dot{l} = 0$. Thus if surface mechanisms are the only sintering mechanisms that are active (i.e., $\dot{V}_{bulk} = 0$), then Eq. 14 reduces to

$$\frac{\partial V}{\partial a} \cdot \dot{a} = \dot{V}_{surf} \tag{15}$$

and Eq. 15 represents the third and final equation in the general sintering model.

The two surface transport mechanisms included in the sintering model are surface diffusion and volume diffusion on the surface (Equations 5 & 6), therefore

$$\dot{V}_{surf} = \dot{V}_{sd} + \dot{V}_{vds} \tag{16}$$

and similarly for the bulk mechanisms, volume and grain boundary diffusion (Equations 7 & 8), thus

$$\dot{V}_{bulk} = \dot{V}_{vd} + \dot{V}_{gbd} \tag{17}$$

Equations 11, 14, and 15 creates a system of two differential equations and one algebraic equation that are used to solve the change in neck volume driven by the two surface and two bulk mechanistic volumetric fluxes. Equations 16 and 17 indicate the surface and bulk mechanisms included in the general sintering model, represented by

$$\frac{\partial V}{\partial a} \cdot \dot{a} + \frac{\partial V}{\partial l} \cdot \dot{l} = \dot{V}_{sd} + \dot{V}_{vds} + \dot{V}_{vd} + \dot{V}_{gbd} \tag{18a}$$

$$\frac{\partial V}{\partial a} \cdot \dot{a} = \dot{V}_{sd} + \dot{V}_{vds} \tag{18b}$$

$$V_{sys}(a, \rho, l) = V_{sys}(a_o,\ \rho_o,\ l_o) \tag{18c}$$

In order to reduce the mathematical complexity in the general sintering model, Eq. 18b is subtracted from Eq. 18a, which reduces the system of equations to

$$\frac{\partial V}{\partial a} \cdot \dot{a} = \dot{V}_{sd} + \dot{V}_{vds} \tag{19a}$$

$$\frac{\partial V}{\partial l} \cdot \dot{l} = \dot{V}_{vd} + \dot{V}_{gbd} \tag{19b}$$

$$V_{sys}(a, \rho, l) = V_{sys}(a_o,\ \rho_o,\ l_o) \tag{19c}$$

The complicated functional form of the partial derivatives and the material flow rates makes an analytical solution unfeasible, but numerical solutions of this system of constrained first order ODE's can be readily computed. We employed *Mathematica*'s constrained ODE solver to obtain the simulation results presented herein.

In order to completely define the system, initial geometric conditions are required for $a$, $\rho$, and $l$. The initial particle radius ($a_o$) is defined to be the mean radius of the powder particles ($a_m$) obtained from a particle diameter analysis, i.e., $a_o = a_m$. The powder is loosely compacted after manufacturing and possesses no particle flattening (or penetration), therefore the initial separation is just the initial particle radius, i.e., $l_o = a_o$. An initial neck radius is produced from metallic bonding forces associated with a Hertzian contact. Easterling [8, 9]

and German [2], have defined a method to calculate the initial neck radius ($\rho_o$) depending on the free surface area consumed by the contact geometry of the two spheres, which has been calculated to be, $\rho_o = 10^{-3} a_o$, and is the same value used by Hwang [6]. Therefore, the complete geometric initial conditions are represented by

$$(a_o,\ \rho_o,\ l_o) = (a_m,\ 10^{-3} a_m,\ a_m) \tag{20}$$

The mechanistic fluxes (Equations 5-8) are temperature dependant (i.e., $\dot{V}_i \equiv \dot{V}_i(a, \rho, l, T)$) and the system of equations represented by Eq. 19 (with initial conditions displayed in Eq. 20) can be solved under an applied temperature profile $T_{profile}$.

## 4.2 Sintering Model Calibration

The final version of the general sintering model (Section 4.1) uses the accepted values of the material constants for 316L SS, displayed in Table 2. Material constant values are not precisely established, but possess an accepted range of values and a choice was made to combine the variability of the material constant values into a single numeric coefficient ($B_i$) for each mechanism. Past researchers [2, 1, 3, 5, 10] have performed similar analyses to address this issue which have resulted with a range of values for the numeric coefficients $\vec{B}_i$, shown in Table 3. Powder particles with mean diameter of 80 $\mu$m were used, (i.e., $a_m = 40\mu$m).

Table 3: Value range for numeric coefficients of sintering mechanisms and the optimal values obtained from dilatometry calibration.

| Mechanism | Numeric Coefficient ($B_i$) | Numeric Coefficient Range* | Optimal Value |
|---|---|---|---|
| Volume Diffusion | $B_{vd}$ | 8 - 80 | 42 |
| Grain Boundary Diffusion | $B_{gbd}$ | 20 - 48 | 18 |
| Surface Diffusion | $B_{sd}$ | 23 - 56 | 0.7 |
| Volume Diffusion on the Surface | $B_{vds}$ | 1 - 80 | 0.9 |

*Isothermally determined by previous researchers [2, 3, 10]

In order to calibrate the strain predictions from the sintering model (Equations 19 with initial conditions in Eq. 20), the model was calibrated using a data set of non-isothermal dilatometer strain measurements [15]. The experimental data set of dilatometer measurements employed four different heating rates (4-20°C/min) to reach five different maximum temperatures (1010-1263°C) which encompassed the various industrial sintering processing conditions for 316L SS. These sintering responses provide data to support and calibrate the sintering model presented in Section 4.1. Optimal values for $\vec{B}_i$ (listed in Table 3) were determined by minimizing the sum of the squared error between the sintering model strain predictions and the dilatometer strain measurements under this set of sintering temperature profiles that include both non-isothermal and isothermal conditions. The optimal values for the numeric coefficients (displayed in Table 3) show that the values for the bulk mechanisms are close to the isothermally determined coefficients.

Using the optimal coefficients, the sintering model is accurate to within 20.3±5.9% of the experimentally measured final strain for the calibration data set, which has a temperature

Table 4: Average relative error for the final sintering strain predictions of the sintering model using the optimal coefficients $(B_{vd}, B_{gbd}, B_{sd}, B_{vds}) = (42,\ 18,\ 0.7,\ 0.9)$ compared to the dilatometer strain measurements.

| Sintering Temperature Range | Average Relative Strain Error (%) | 90% Confidence Interval |
|---|---|---|
| 1010-1263°C | 20.3 | 20.3±5.9% |
| 1100-1250°C | 10.7 | 10.7±5.2% |

range of 1010-1263°C. Sintering of 316L SS is predominantly performed in the temperature range of 1180-1250°C [2], and the model increases in accuracy to 10.7±5.2% of the experimentally measured final strain compared to the calibration data set (90% confidence interval).

## 4.3 Dilatometer testing of optimized sintering model

Predictive capabilities of the optimized sintering model were evaluated by performing additional dilatometer experimentation using various temperature profiles not included in the calibration data set. Two of the test temperature profiles possessed a minimally different heating rate and isothermal sintering temperature than the dilatometer calibration data set. The remaining test temperature profiles exhibited unorthodox heating profiles to test the robustness of strain predictions calculated by the sintering model. The graphical results of the evaluation temperature profiles are shown in Figure 3 which include the temperature profiles, the strain calculated by the sintering model compared to the measured strain with no thermal expansion effects, and the computed predicted and measured strain rates. All of the verification temperature profiles used the same binder elimination interval at the beginning of the temperature profile. A brief summary of the test temperature profiles is provided in Table 5 and graphical results for tests 1 and 4-6 are shown in Figure 3.

Table 5: Summary of dilatometer temperature profile tests of the sintering model. The temperature profile and strain results for tests 1 and 4-6 are shown in Figure 3.

| Test | Test Characteristics | Relative Strain Error (mm/mm) | Percent Strain Error (%) |
|---|---|---|---|
| Test 1 | Heating rate 5°C/min, $T_{max} = 1240$°C | 0.0149 | 23.2 |
| Test 2 | Heating rate 2°C/min, $T_{max} = 1250$°C | 0.0187 | 41.1 |
| Test 3 | Temp. spike during isothermal interval | -0.0097 | 16.6 |
| Test 4 | Mixed heating and isothermal intervals | -0.0122 | 17.0 |
| Test 5 | Mixed heating and cooling intervals | -0.0074 | 10.9 |
| Test 6 | Two heating and isothermal intervals | 0.0007 | 0.9 |
| | Average | 0.00083 | 18.3 |
| | Standard Deviation | 0.01316 | 13.5 |

The sintering model was accurate to within 18.3±5.5% of the final strain measured experimentally for the dilatometer test temperature profiles, within a 90% confidence interval. The strain rates computed by the sintering model qualitatively show all the relevant rate changes

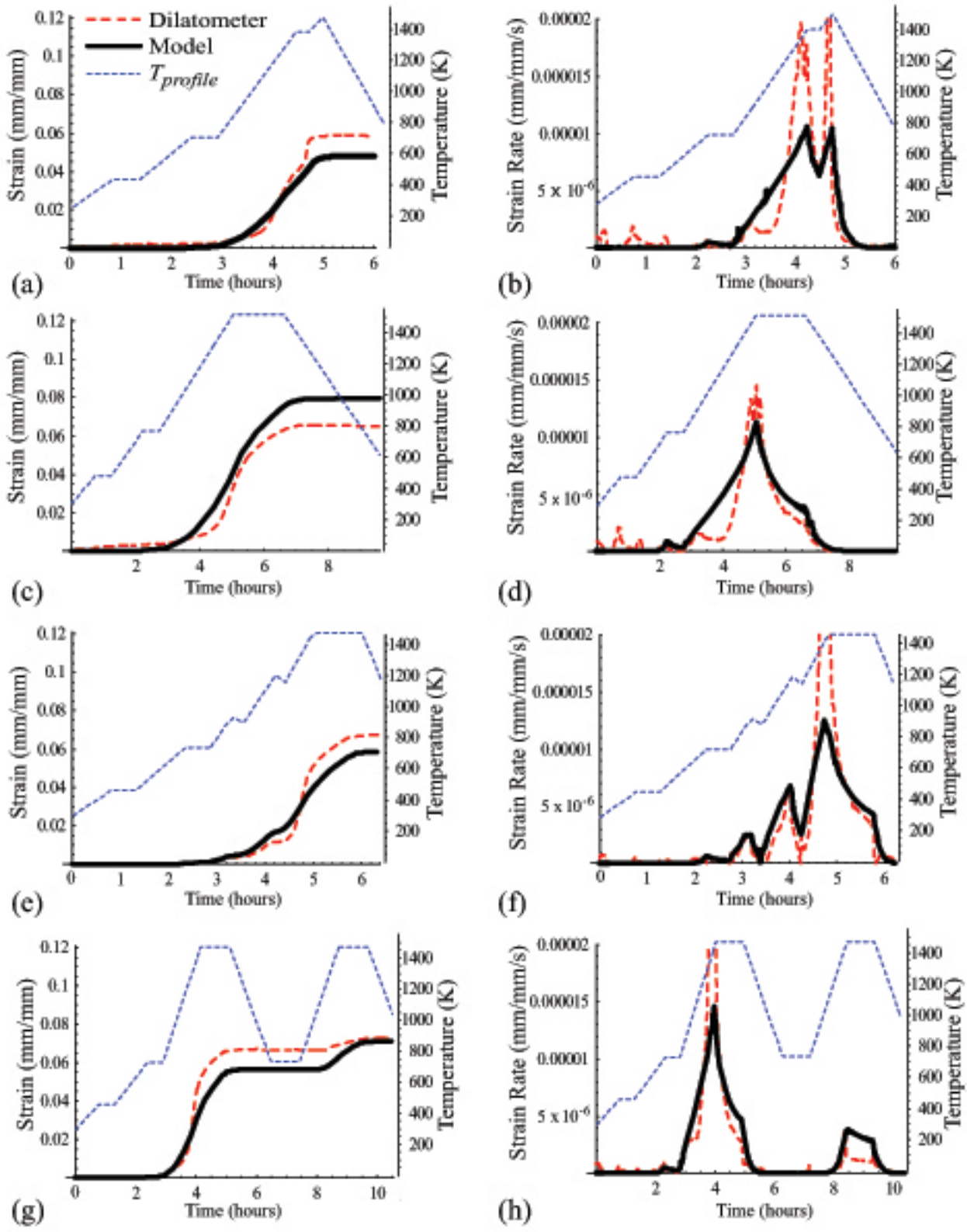


Figure 3: Dilatometer testing of sintering model for defined temperature profiles mentioned in Table 5. Left column displays measured strain values and the right column shows the computed strain rates. (a-b) Test 1, (c-d) Test 4, (e-f) Test 5, and (g-h) Test 6.

during heating compared to the measured strain rates, shown in Figure 3d, f, & g. The sintering model is able to predict the changes in the strain rates related to the temperature changes resulting from each temperature profile.

# 5 Conclusions

The sintering model developed in this paper and presented as Eq. 19 is applicable for isothermal and non-isothermal sintering conditions. Instantaneous strain predictions (in-sintering) predicted by the sintering model compared to dilatometry experimentation during the heating and isothermal intervals had an average percentage error of 20-65%. The sintering model produces accurate strain predictions to within 10% of experimental measurements using the optimized coefficients for $\vec{B}_i$ over standard sintering temperatures for 316L SS. The sintering model thus improves upon the accuracy of previous sintering models that were at best accurate in strain prediction within a factor of two [1].

Past sintering strain models were developed primarily under isothermal sintering conditions using rapid heating rates to reach elevated temperatures. The equations describing the mechanistic fluxes presented by Ashby [1] were developed from isothermal theory using rapid heating rates, which accounts for the sintering model's ability to reproduce sintering strain rates using faster heating rates and is less accurate for when using slow heating rates. The sintering model was able to most closely predict the in-sintering strain for dilatometry experimentation using heating rates of 7-20°C/min with maximum sintering temperatures ranging from 1100-1230°C, which possessed average relative errors of 20-38%. The sintering model can qualitatively reproduce features of the sintering strain rate during heating intervals using a heating rates of 10-20°C/min. Isothermal sintering strain rates are accurately predicted at temperatures from 1100 to 1230°C independently of prior heating rates. Furthermore, the sintering model quantitatively models final strain for temperature profiles using various heating rates and isothermal intervals within 18.3±5.5% of the experimentally measured final strain. Additionally, the optimal values for the $\vec{B}_i$ surface mechanisms do not correspond to the isothermally determined coefficient ranges shown in Table 3, which is reasonable since the optimal $\vec{B}_i$ values were determined under both isothermal and non-isothermal sintering conditions.

Some of the possible geometric contributions to strain errors in the sintering model are: (1) powder particles are not perfectly spherical, (2) adjacent particles are rarely the same diameter, (3) particles do not remain perfectly spherical during sintering, (4) the neck geometry does not remain spherical, and (5) there is particle erosion at the particle-to-neck interface. Formulating an exact geometric model of neck growth between two particles is challenging and would require an additional geometric description of neck growth geometry.

The mechanistic flux usage in the sintering model allows for mechanism interaction that closely resembles actual sintering. Mechanisms have been linked to geometric parameter rates (Equations 19a & 19b) in the ideal two particle geometry for volumetric neck growth rates simulated by the optimized sintering model.

# References


[1] F.B. Swinkels and M.F. Ashby. A second report on sintering diagrams. *Acta Metallurgica*, 29:259–281, 1981.

[2] R.M. German. *Sintering Theory and Practice*. Wiley & Sons, New York, 1996.

[3] H.E. Exner. Principles of single phase sintering. *Reviews on Powder Metallurgy and Physical Cermaics*, 1(1-4):11–251, 1979.

[4] M.F. Ashby. A first report on sintering diagrams. *Acta Metallurgica*, 22:275–289, March 1974.

[5] D. Lynn Johnson. New method of obtaining volume, grain boundary, and surface diffusion coefficients from sintering data. *Journal of Applied Physics*, 40(1):192–200, January 1969.

[6] K.S. Hwang, R.M. German, and F.V. Lenel. Analysis of initial stage sintering through computer simulation. *Powder Metallurgy International*, 23(2):86–91, April 1991.

[7] S. Brennom and D.L. Johnson. Non-isothermal initial stage sintering of silver. *Materials Science Research*, 6:269–274, 1973.

[8] K.E. Easterling and A.R. Thölén. Surface energy and sintering. *Physics of Sintering*, 1:77–84, 1971.

[9] K.E. Easterling and A.R. Thölén. Surface energy and adhesion at metal contacts. *Acta Metallurgica*, 20:1001–1008, August 1972.

[10] R.M. German. *Powder Metallurgy Science*. Metal Powder Industries Federation, Princeton, NJ, 1984.

[11] G.C. Kuczynski. Self-diffusion in sintering of metallic particles. *Transactions of the American Institute of Mining, Metallurgical and Petroleum Engineers*, 185:169–78, 1949.

[12] W.D. Kingery and M. Berg. Study of the initial stages of sintering solids by viscous flow, evaporation-condensation, and self diffusion. *Journal of Applied Physics*, 26(10):1205–1212, Oct. 1955.

[13] G.C. Kuczynski. Study of the sintering of glass. *Journal of Applied Physics*, 20:1160–1163, Dec. 1949.

[14] F. Thummler and R. Oberacker. *An Introduction to Powder Metallurgy*. The University Press, Cambridge, 1993.

[15] S. Johnston. *Initial Stage Sintering Model of 316L Stainless Steel with Application to Three Dimensionally Printed Components*. PhD thesis, University of Washington, Seattle, WA, June 2005.